Title
Anisotropy-Driven Crystallization of Dimensionally Resolved Quasi-1D Van der Waals Nanostructures.

Journal
Journal of the American Chemical Society, 145(41)

Authors
Cordova, Dmitri
Chua, Kenneth
Huynh, Rebecca
et al.

Publication Date
2023-10-18

DOI
10.1021/jacs.3c05887

Peer reviewed

JACS
JOURNAL OF THE AMERICAN CHEMICAL SOCIETY

pubs.acs.org/JACS
Article

Anisotropy-Driven Crystallization of Dimensionally Resolved Quasi-1D Van der Waals Nanostructures

Dmitri Leo Mesoza Cordova, Kenneth Chua, Rebecca Mai Huynh, Toshihiro Aoki, and Maxx Q. Arguilla*

Cite This: J. Am. Chem. Soc. 2023, 145, 22413−22424
Read Online

ABSTRACT: Unusual behavior in solids emerges from the complex interplay between crystalline order, composition, and dimensionality. In crystals comprising weakly bound one-dimensional (1D) or quasi-1D (q-1D) chains, properties such as charge density waves, topologically protected states, and indirect-to-direct band gap crossovers have been predicted to arise. However, the experimental demonstration of many of these nascent physics in 1D or q-1D van der Waals (vdW) crystals is obscured by the highly anisotropic bonding between the chains, stochasticity of top-down exfoliation, and the lack of synthetic strategies to control bottom-up growth. Herein, we report the directed crystallization of a model q-1D vdW phase, Sb_2S_3, into dimensionally resolved nanostructures. We demonstrate the uncatalyzed growth of highly crystalline Sb_2S_3 nanowires, nanoribbons, and quasi-2D nanosheets with thicknesses in the range of 10 to 100 nm from the bottom-up crystallization of $[Sb_4S_6]_n$ chains. We found that dimensionally resolved nanostructures emerge from two distinct chemical vapor growth pathways defined by diverse covalent intrachain and anisotropic vdW interchain interactions and controlled precursor ratios in the vapor phase. At sub-100 nm nanostructure thicknesses, we observe the hardening of phonon modes, blue-shifting of optical band gaps, and the emergence of a new high-energy photoluminescence peak. The directional growth of weakly bound 1D ribbons or chains into well-resolved nanocrystalline morphologies provides opportunities to develop ordered nanostructures and hierarchical assemblies that are suitable for a wide range of optoelectronic and quantum devices.

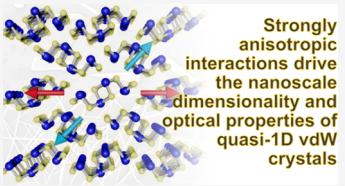

INTRODUCTION

Physical properties of solids are inherently coupled to their structure and dimensionality. As a consequence, the discovery of complex and exotic phenomena in condensed phases has incessantly relied upon the creation of well-defined structures in low dimensions.[1−11] The realization of monolayers from two-dimensional (2D) subunits held together by weak van der Waals (vdW) interactions, such as in graphene and transition metal dichalcogenides, has redefined the way stable and well-defined crystalline structures approaching the subnanometer regime are created.[3−5,12,13] These monolayers, due to their size and dimensionality, have enabled the demonstration of nascent physical and quantum phenomena including room-temperature quantum Hall effect in graphene,[14,15] indirect-to-direct gap crossover in MoS_2,[3] unusual superconductivity in twisted vdW bilayers,[16] complex topological spin textures,[12,17] valleytronics,[3,18] and single-photon emission.[19] This foregoing notion that extended lattices can be separated into subnanometer monolayers that display drastically altered physical properties has advanced the phase space exploration toward new classes of 2D vdW materials with varying degrees of anisotropies, electronic correlations, and levels of atomic-scale structural complexity.

The conceptual understanding of weak vdW interactions in 2D materials has led to the discovery of unusual electronic landscapes such as in moiré, hierarchical, and Eshelby twisted structures, as well as methodologies that allow for the direct synthesis of substrate-scale 2D monolayers.[11,20−23] More recently, immense efforts have been made toward accessing even lower dimensionalities—as one-dimensional (1D) analogues of 2D vdW phases—via routes such as substrate engineering,[20,23] controlled catalyzed growth,[21,22] and confined syntheses.[24] These methods have resulted in well-defined 1D nanostructures that display emergent electronic states that challenge the limits of solid-state confinement. Still, the fundamental limit of covalent bonding in two dimensions substantially hinders the realization of 1D structural confinement in 2D vdW phases to lateral dimensions in the nanometer regime. Inspired by how vdW interactions in 2D materials enable the realization of ultrathin and confined nanostructures, recent studies have shown that the same, weak, vdW interactions can exist between atomically precise 1D or quasi-1D (q-1D) chains with lateral dimensions approaching the subnanoscale.[2,6,7] Because of the strong confinement in 1D, stacking-dependent higher-order topological states,[25−27] high-

Received: June 5, 2023
Published: September 15, 2023

https://doi.org/10.1021/jacs.3c05887
J. Am. Chem. Soc. 2023, 145, 22413−22424

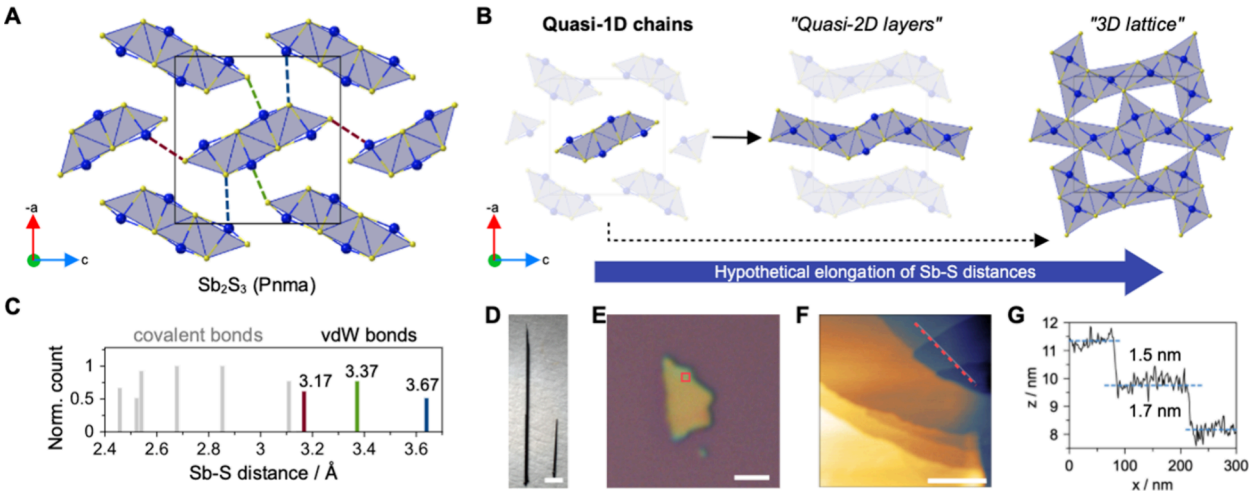

Figure 1. Anisotropic interchain interactions in the model q-1D vdW crystal, Sb_2S_3. (a) Crystal structure representation of the q-1D vdW model phase, Sb_2S_3. The unit cell is enclosed by a black box and select interchain Sb···S distances are depicted as red (shortest), green, and blue (longest) dashed lines. Sb atoms are depicted in blue, while sulfur atoms are depicted in yellow. (b) Hypothetical elongation of the Sb···S distances in the crystal structure models. (c) Histogram of intra- and interchain Sb−S bond distances derived from the Sb_2S_3 unit cell. Intrachain distances (covalent bonds) are depicted in gray bars, while interchain distances (vdW bonds) are depicted in red, green, and blue bars. The heights of these bars correspond to the number of similar distances found within the unit cell. These interchain vdW interactions correspond to the distances (in dashed lines with the same colors) in panel a. (d) Sizeable single crystals of Sb_2S_3. Scale bar: 1 mm. (e) Optical micrograph of micromechanically exfoliated Sb_2S_3 on Si/SiO_2. The red box indicates the region probed in panel g. Scale bar: 5 μm. (f, g) AFM and the corresponding height profile of the line cut taken from the Sb_2S_3 nanoflake in panel e. The dotted red line in panel f indicates the z-height plotted in panel g. Scale bar: 200 nm. Dashed lines were added as guides to emphasize the layer steps found in the micrograph.

fidelity electrical transport,[28] unusual superconductivity,[26] and Dirac polarons[29] have been experimentally demonstrated to exist in these 1D or q-1D vdW phases.

However, as in 2D vdW materials, the discovery of emergent properties of single chains or few-chain-thick bundles is obscured by the stochastic nature of micromechanical or solution-phase exfoliation of bulk crystals. As such, top-down routes to access 1D or q-1D vdW nanostructures yield a broad distribution of lengths and thicknesses that are observed in nanowire bundles, nanoribbons, and quasi-2D nanosheets.[30−34] Beyond the stochasticity of top-down exfoliation, the strong influence of nonequivalent basal plane interchain interactions perpendicular to the long axis further complicates this process. As a result, it has been historically challenging to produce uniform nanostructures from top-down exfoliation.[2,31] While several strategies have been attempted to access nanoscale 1D and q-1D phases from bottom-up,[35−39] methods of controlled synthesis of well-defined nanostructures derived from 1D and q-1D vdW materials are still severely underdeveloped.

In this report, we demonstrate that anisotropic intra- and interchain interactions in a model q-1D vdW crystal, Sb_2S_3, can be harnessed to direct the synthesis of dimensionally resolved nanostructures. We show that well-defined and highly crystalline nanowires, nanoribbons, and quasi-2D nanosheets with thicknesses in the 10 to 100 nm range can be grown from the bottom-up through an uncatalyzed vapor growth route. The synthetic methodology that we developed enabled us to obtain a panoramic view of diverse nanostructures under discrete synthetic conditions, which relied on our ability to tune outgoing vapor compositions using precursor preconcentration and shuttling, and the application of a large temperature gradient along the substrate. Photoluminescence (PL) studies of individual nanocrystals show the systematic size-dependent blue-shifting of the indirect gap peak and the emergence of a distinct high-energy PL emission in sub-100 nm-thick nanocrystals. This emergent feature is a result of confinement along the crystallographic [001] direction and is consistent with the size-dependent commencement of an indirect-to-direct band gap transformation. Finally, we identified two unique growth pathways based on the interplay of the covalent and anisotropic interchain interactions in Sb_2S_3. We illustrated how these two growth pathways are correlated with the resulting crystal habits and facets along the low-index [010], [100], and [−101] directions observed in the nanocrystals. We believe that the synthetic strategy that we implemented herein is one that could be generalized to access nanostructures based on several emergent classes of 1D and q-1D vdW phases as well as 2D vdW phases that display strong 1D in-plane motifs. With the strategies that we presented, we gain a general understanding of size- and dimension-dependent physics in a unique class of 1D solids that could be leveraged toward downstream applications in photonics and excitonics.

RESULTS AND DISCUSSION

Interchain Bonding Anisotropy in the Sb_2S_3 Crystal Structure. Our ability to control the crystallization of 1D or q-1D vdW nanostructures relies on a phase composed of weakly bound chains with an anisotropic cross section and several unique chemical identities along the chain surface. As such, we focused on Sb_2S_3, a q-1D vdW phase that belongs to a family of earth-abundant Pn_2Ch_3 pnictochalcogenides (Pn = pnictogen, e.g., Sb and Bi; and Ch = chalcogen, e.g., S and Se) (Figure 1). These phases have been heavily studied due to their optical and electronic properties, which include visible-to-near-infrared band gaps reported in the 1.1 to 1.8 eV range and substantial optical absorption coefficient suitable for thin-film solar energy conversion devices.[40−42] More recently, studies have shown that the photovoltaic efficiencies of thin films based on Sb_2S_3 are strongly dependent on the crystallographic

https://doi.org/10.1021/jacs.3c05887
J. Am. Chem. Soc. 2023, 145, 22413−22424

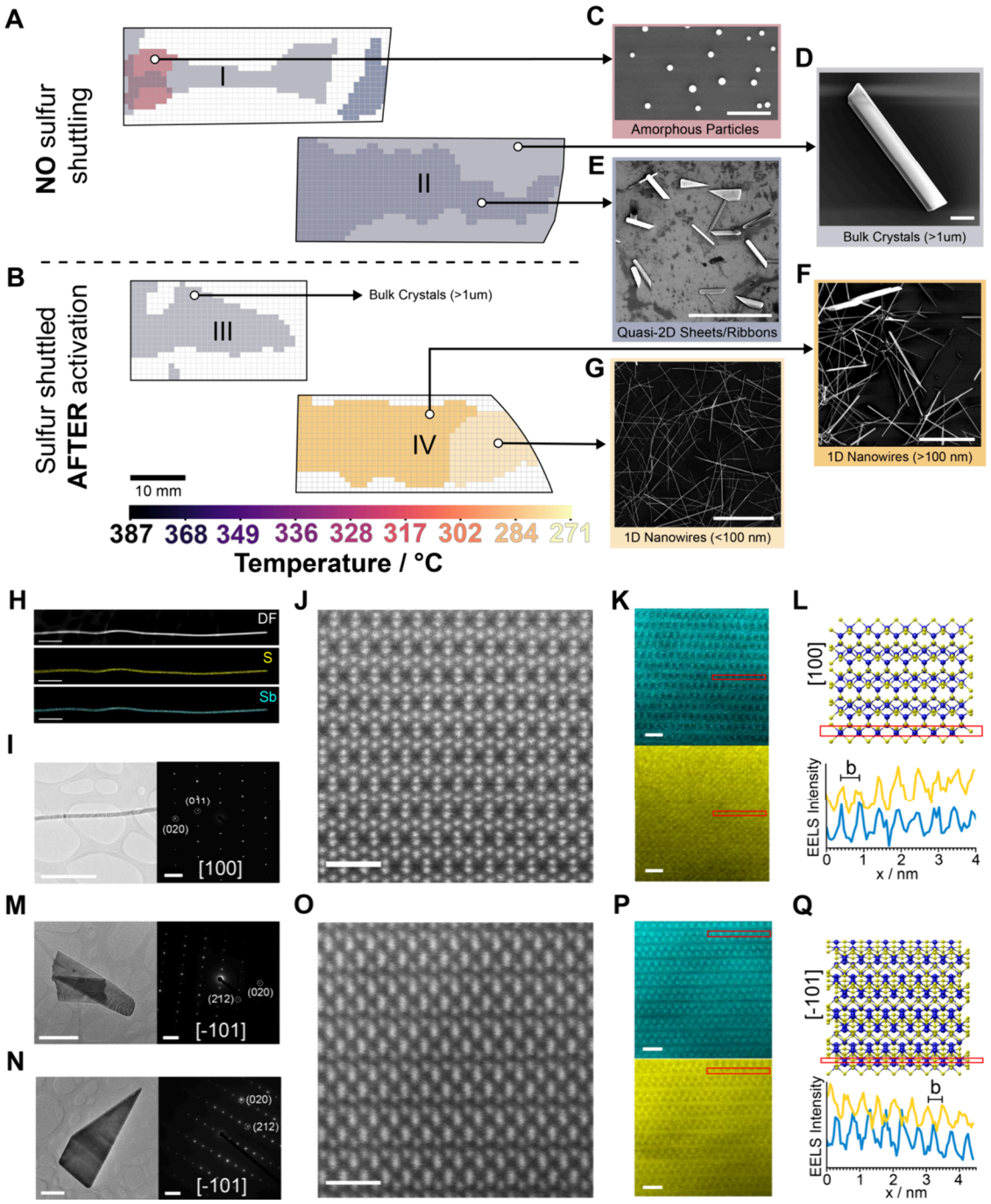

Figure 2. Synthesis and structure of dimensionally resolved nanocrystal structures of a model q-1D vdW phase, Sb_2S_3. (a, b) Panoramic synthesis of Sb_2S_3 nanostructures with (a) and without (b) sulfur shuttling. Substrate labels I–IV indicate the deposition behavior at different conditions. (c–g) Representative SEM structures spatially mapped with 1 mm resolution with respect to the calibrated temperature in the deposition zone. The color of the box that contains the SEM image corresponds to the morphology of the majority nanostructure deposited in each 1 × 1 mm^2 section of substrates I–IV. Substrate boundaries are defined by the black lines, and areas in white correspond to empty regions with no noticeable material deposition. Scale bar, 10 μm. Note that the structures in panel e originally grew vertically and were flattened using a PDMS stamp for better visualization. (h) STEM image (top) of a Sb_2S_3 nanowire with its corresponding S (middle) and Sb (bottom) elemental EDS maps. Scale bar: 1 μm. (i) TEM image of a Sb_2S_3 nanowire (Scale bar: 1 μm) with its corresponding SAED pattern (Scale bar: 2 nm^{-1}). (j) HAADF-STEM image of a Sb_2S_3 nanowire. Scale bar: 1 nm. (k) EELS map of the Sb *M*-edge (top, blue) and S *L*-edge (bottom, yellow) corresponding to the micrograph in panel j. Scale bar: 1 nm. (l, top) Crystal structure of Sb_2S_3 along the crystallographic [100] zone axis. (l, bottom) EELS intensity line profile from a section of the map (enclosed in a red rectangle). (m, n) TEM image of a Sb_2S_3 quasi-2D nanoribbon cut in half and quasi-2D nanosheet (left; Scale bar: 1 μm) with their corresponding SAED pattern (right; Scale bar: 2 nm^{-1}). (o) HAADF-STEM image of a representative Sb_2S_3 nanosheet. Scale bar: 1 μm. Zone axes indexed from the SAED patterns (m, n, right) correspond to the facets normal to the electron beam in the TEM images (m, n, left). (p) EELS map of the Sb *M*-edge (top, blue) and S *L*-edge (bottom, yellow) corresponding to the micrograph in panel o. Scale bar: 1 nm. (q) Crystal structure model of Sb_2S_3 along the [−101] zone axis (top) and EELS intensity line profile from a section of the map. The atoms enclosed by the red rectangle on the crystal structure models (l, q, top) correspond to the red rectangle in the EELS map (k, p) and the EELS profile (l, q, bottom). For l and q, *b* corresponds to the crystallographic *b*-lattice parameter length.

https://doi.org/10.1021/jacs.3c05887
J. Am. Chem. Soc. 2023, 145, 22413–22424

orientation of the polycrystalline domains, implying that the physical properties of these pnictochalcogenides are inherently tied to their morphologies and nanocrystalline structures.[43−46] Encouragingly, numerous computational studies have predicted the size- and orientation-dependent indirect-to-direct band gap crossover in Sb_2S_3 upon confinement due to the small energy differences in the conduction band states along and across the chains.[47−51]

The crystal structure of Sb_2S_3 can be described as an array of q-1D chains of $[Sb_4S_6]_n$. These chains have sub-nm cross sections and are stacked together through weak interchain interactions in an orthorhombic, *Pnma*, unit cell (Figure 1a).[52] Projection of the structure along the crystallographic *b*-axis (long axis) highlights the vdW-like nature of the chains, which suggests that Sb_2S_3 can be micromechanically exfoliated into single chain structures, as is the case for typical 2D vdW crystals. However, unlike 2D vdW crystals that possess equivalent interlayer interactions across adjacent layers, close inspection of the Sb_2S_3 crystal structure reveals that the nearest neighbor interchain Sb···S distances, which are typically denoted as purely "vdW" interactions, are not equivalent.[52,53] From a top-down exfoliation perspective, this means that crystallographic axes along interchain directions with weaker interactions (i.e., longer interatomic or interchain distances) will be easier to exfoliate compared to those with stronger interactions.

We hypothetically elongated the Sb−S bonds in the crystal structure model (Figure 1b) and extracted the interchain (vdW or close to vdW) and intrachain (covalent) Sb···S distances from the structure to visually demonstrate this concept (Figure 1c). From this schematic, the elongation of the bonds illustrates that the structure does not directly transform into a hypothetical 3D network lattice. Instead, the hypothetical model transitions first into quasi-2D sheets comprising chains oriented along the [001] direction. This structural anisotropy originates from the significantly shorter interchain distances (3.17 Å versus 3.37 and 3.67 Å) along the crystallographic *z*- or *c*-direction ([001] direction). This observation aligns with several first-principles and crystallography studies that described the propensity of the terminal stereochemically active Sb 5s lone pairs at the ends of the chains to interact with S 3p states of the adjacent chains along the [001] direction.[53−55] Experimentally, we grew bulk single crystals of Sb_2S_3 and carried out micromechanical exfoliation using a polydimethylsiloxane (PDMS) stamp to illustrate the influence of the interchain bonding anisotropy on the resulting top-down-derived nanostructures. The sizable bulk crystals grown via melt synthesis showed long, needle-like morphologies, consistent with the q-1D motif in the crystal structure (Figure 1d). Contrary to the expected exfoliation into nanowires, as prescribed by the q-1D crystal structure and bulk crystalline habit, micromechanical exfoliation of these needle-like bulk crystals resulted in nanosheets (Figure 1e,f). These well-defined quasi-2D sheets are reminiscent of exfoliated 2D vdW crystals, with terrace *z*-heights approaching unit cell thicknesses (Figure 1g). The exfoliation of Sb_2S_3 appears to consistently result only into quasi-2D sheets regardless of the exfoliation method either micromechanically, as demonstrated, or in the liquid phase.[30,33,34]

Chemical Vapor Deposition Synthesis of Sb_2S_3 nanostructures. With the influence of interchain interactions established, we used bottom-up chemical vapor deposition (CVD) routes to ascertain synthetic parameters that could leverage this intrinsic anisotropy to grow dimensionally resolved q-1D vdW nanostructures (Figure 2, Figures S1 and S2, and Table S1). Based on the binary Sb−S phase diagram, Sb_2S_3 is the only thermodynamically stable compound known to form, which minimizes the risk of the formation of unwanted and off-stoichiometric competing phases when grown from the bottom-up.[56,57] We focused on investigating the influence of the vapor Sb:S ratio and deposition temperature on the growth of the resulting nanostructures. In our syntheses, we employed longer (∼3−5 cm) substrates, which enabled us to map the deposition of nanostructures with 1 mm-scale spatial resolution across a wide ∼100 °C calibrated temperature window (Figure 2a−g and Figure S3). Noting the significantly higher vapor pressures of sulfur compared to antimony, we employed a preconcentration step that involves reverse gas flow during the temperature ramp-up and equilibration periods (described in the Supporting Information, Section I). This step ensures a controllable and stable composition ratio of Sb and S in the vapor phase and prevents the premature deposition of any material during the induction period.[58] Upon inspection of the resulting substrates when Sb_2S_3 and S powders were simultaneously heated as precursors (Figure 2a), we found from scanning electron microscopy (SEM) that amorphous spherical particles with 2:3 Sb-to-S ratios (Figure 2c) and the bulk (>1 μm thick) single crystals of Sb_2S_3 (Figure 2d, substrate I) dominate the growth at high temperatures and positions close to the precursor boat. At lower temperatures and farther distances from the precursor boat, we observed the formation of nanoribbons and nanosheets (Figure 2e, substrate II) that closely resembled the quasi-2D structures derived from micromechanical exfoliation.

The modular nature of CVD growth allowed us to further investigate the influence of the vapor-phase elemental ratios on the resulting morphologies of the Sb_2S_3 nanostructures. This was done by shuttling the elemental sulfur into the already heated Sb_2S_3 precursors after the preconcentration period to drastically lower the Sb:S ratio of the incoming vapor just before its deposition to the substrate (Figure 2b). This contrasts with the previous procedure (Figure 2a) wherein both Sb_2S_3 and elemental sulfur were heated simultaneously during the preconcentration step. In conditions that involved the shuttling of elemental sulfur, we still observed the crystallization of bulk Sb_2S_3 in the high-temperature regions around 390−340 °C (Figure 2b, substrate III). Remarkably, at lower temperatures and farther distances from the precursor boat (Figure 2b, substrate IV), we noticed the formation of thick (Figure 2f) and thin (Figure 2g) nanowires (Figure S4). Based on SEM and atomic force microscopy (AFM) imaging, we found that the thicknesses of these nanowires decreased with decreasing temperature and increasing distance from the precursors. These nanostructures are more consistent with the q-1D nature of the $[Sb_4S_6]_n$ chains in Sb_2S_3 and are in stark contrast to the low-temperature growth of quasi-2D nanostructures without additional sulfur shuttling (Figure 2a, substrates I and II).

We performed electron microscopy and diffraction to elucidate the structure and understand the crystallization habit of the resulting 1D and quasi-2D nanocrystals (Figure 2h−q and Figure S5). Scanning transmission electron microscopy (STEM) and energy-dispersive X-ray spectroscopy (EDS) mapping on the nanowires confirmed the large 1D aspect ratios observed and the uniform elemental Sb and S

https://doi.org/10.1021/jacs.3c05887
J. Am. Chem. Soc. 2023, 145, 22413−22424

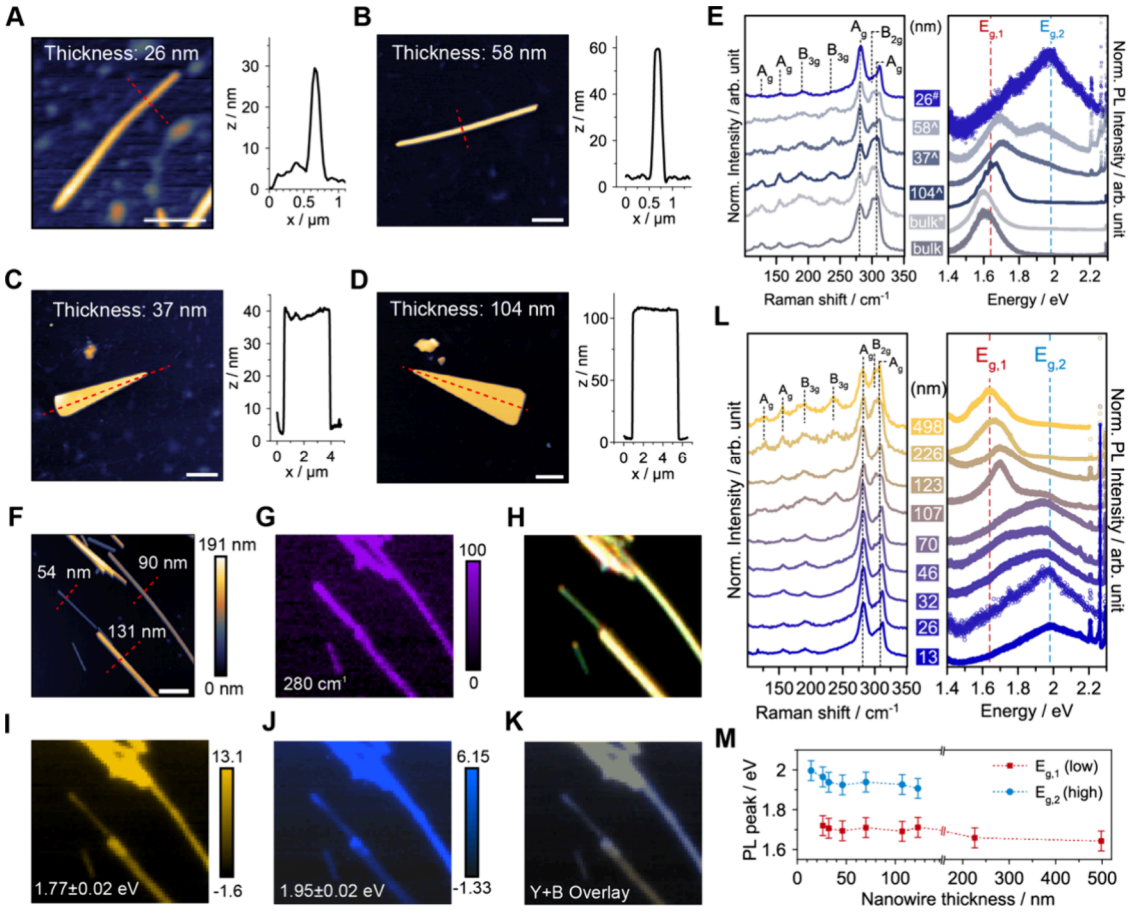

Figure 3. Size- and dimension-dependent spectroscopic signatures of Sb_2S_3nanocrystals. (a–d) AFM topographical map of a representative Sb_2S_3 thin nanowire (a), thick nanowire (b), thin nanosheet (c), and thick nanosheet (d) with their corresponding height profiles. The red dotted lines indicate the regions from which the height profiles were extracted from. Scale bar: 1 μm. (e) Raman (left) and PL (right) spectra of bulk and nanoscale Sb_2S_3 crystals with varying crystal morphologies. The superscript next to the thickness value corresponds to the following morphologies: # for 1D nanowires and ^ for quasi-2D nanosheets. The bulk and bulk* labels correspond to bulk Sb_2S_3 crystals grown via CVD and melt, respectively. The peaks above 2.2 eV are the same Raman-active peaks observed in the left panel. (f) AFM topographical map of a dense nanowire region. The red dotted lines indicate the regions from which the heights were extracted from. Scale bar: 2 μm. (g–k) False color Raman intensity map of the 280 cm^{-1} mode (g), dark-field optical micrograph (h), false color PL map from the peak centered at 1.77 eV (i), false color PL map from the peak centered at 1.95 eV (j), and overlay of panels i and j (k), taken in the same region as the micrograph in panel f. (l) Raman (left) and PL (right) spectra of Sb_2S_3 nanocrystals with nanowire morphologies with various thicknesses to demonstrate size-dependent effects. The thicknesses, in nanometers, are indicated in the space between the two graphs. (m) Plot of the thickness-dependent PL peak energies extracted from panel l. The corresponding phonon modes are indicated in the Raman plots in panels e and l. The red and blue dashed lines corresponding to the low-energy and high-energy PL peaks were added to panels e, l, and m as guides for the eye.

distribution across the length of the nanowire (Figure 2h). Notably, based on SEM, STEM-EDS, and STEM, the absence of spherical, nanoparticle-like features or any distinct grain boundaries at the end of the nanowires precludes a vapor–liquid–solid growth mechanism (Figure S4b–d).[59−61] Bright-field transmission electron microscopy (BF-TEM) and selected-area electron diffraction (SAED) of the Sb_2S_3 nanowires showed that the nanowires are single-crystalline and are indexable to the *Pnma* structure of Sb_2S_3 (Figure 2h). The SAED pattern also indicates that the dominant facets of the nanowires are preferentially oriented along the [100] crystallographic zone axis (Figure 2i), which corresponds to the stacking direction of the quasi-2D sheets previously described (Figure 1b, middle). High-angle annular dark-field scanning transmission electron microscopy (HAADF-STEM) of a representative Sb_2S_3 nanowire demonstrates the high crystalline quality of the resulting nanostructures, as evidenced by the consistent ordering of the Sb and S atoms across the field of view (Figure 2j). In these micrographs, regions of high and low contrasts correspond to Sb and S atoms, respectively. The micrograph can be interpreted as having vertically oriented dumbbell-like features comprised of Sb atoms occupying the *Sb1* position (*4c* Wyckoff site), as well as horizontal zigzag features, which correspond to Sb atoms in the *Sb2* position (*4c* Wyckoff site).[52] Consistent with the indexed SAED pattern, the direct matching of the real space crystal structure (100) Miller plane and the indexing of the fast Fourier transform (FFT) of the HAADF-STEM micrographs both confirm that the exposed facet of the nanowires is oriented along the [100] zone axis (Figure S5a).

High-resolution electron energy loss spectroscopy (EELS) verified the uniform elemental composition of the resulting Sb_2S_3 nanowires (Figure 2k,l and Figure S6). From EELS measurements, the mapping of the Sb *M*-edge (Figure 2k, top) and the S *L*-edge (Figure 2k, bottom) was found to directly match the high- and low-contrast regions of the corresponding

https://doi.org/10.1021/jacs.3c05887
J. Am. Chem. Soc. 2023, 145, 22413−22424

HAADF-STEM image (Figure S5a). Furthermore, we show that the representative line cut (enclosed in a red rectangle) in the crystal structure model oriented along the [100] direction agrees very well with the height variation and peak distances of the EELS intensity profile extracted from the map, which corroborates the staggering of the Sb and S atoms along the [100] zone axis (Figure 2l). These results confirmed both the compositional and structural uniformities of the Sb_2S_3 nanowires. The results from X-ray photoelectron spectroscopy, grazing incidence XRD, and SEM-EDS of as-grown nanowire ensembles indicated good surface stability and confirmed that the structure and composition are consistent with bulk (Figures S7−S10 and Tables S2−S4).

Similarly, we characterized the structure and elemental composition of the quasi-2D nanoribbons and nanosheets (Figure 2m−q, Figure S11, and Table S5). Through the combination of TEM (Figure 2m,n, left), SAED (Figure 2m,n, right), and HAADF-STEM (Figure 2o and Figure S5b), we found that the surfaces of the quasi-2D nanoribbons and nanosheets were oriented along the [−101] zone axis. The linear cut profile (Figure 2q) shows the consistent alternating pattern of the Sb and S atoms from the HAADF-STEM (Figure 2o) and EELS maps (Figure 2p,q), which corresponds very well to the real space crystal structure oriented along the [−101] direction. Intriguingly, this orientation in Sb_2S_3 nanostructures introduces an *x*- and *z*-axis component to the stacking of the $[Sb_4S_6]_n$ chains, in contrast with the preferred and commonly observed [100] orientation of the nanowires. This orientation, however, could also be observed in nanowires but was not as apparent because of the significantly smaller facets compared to the [100]-oriented facets. We also noticed the emergence of diffraction spots equidistant from the direct beam and the (020) reflection in the SAED patterns of the nanoribbons and nanosheets (Figure 2m,n, right). These spots, which could be indexed as part of an odd-numbered (0*k*0) plane, are expected to be systematically absent in the orthorhombic *Pnma* unit cell of Sb_2S_3. These peaks were observed because of double diffraction of strongly diffracting spots adjacent to these peaks. Often occurring in the electron diffraction of highly crystalline nanostructures, these double diffraction peaks further substantiate the high degree of crystallinity of the nanoribbons and nanosheets.[62]

Spectroscopic Characterization of Sb_2S_3 nanowires and Quasi-2D Nanosheets. Beyond the demonstration of the directional and anisotropic growth of a model q-1D vdW phase, the synthesis of Sb_2S_3 nanowires, nanoribbons, and nanosheets with various thicknesses further enabled us to understand the systematic size- and dimension-dependent evolution of its photophysical properties (Figure 3). Based on the on-substrate panoramic maps of the nanostructures grown with and without sulfur shuttling (Figure 2), we characterized representative thick and thin nanowires and quasi-2D nanoribbons (Figure 3a−d). Raman spectroscopy of these nanostructures showed seven characteristic phonon modes of Sb_2S_3 in the 100 to 350 cm^{-1} spectral region corresponding to as-labeled A_g, B_{2g}, and B_{3g} symmetry modes (Figure 3e, left). The observed phonon modes in the nanoribbons and nanosheets are consistent with the Raman-active modes of bulk Sb_2S_3 that we have grown via melt or CVD, as well as those reported in the literature.[63,64] The observation of these Raman-active peaks further confirms the persistence of the orthorhombic *Pnma* structure in the nanowires and nanosheets and complements the structural determination from electron microscopy and diffraction.

The low-energy region of the Raman spectra systematically revealed the dimension- and thickness-dependent evolution of the room-temperature PL emission signature of the nanostructures (Figure 3e, right). Comparing the PL of the nanostructures with the bulk, we observe the consistent blue-shift of the low-energy PL peak ($E_{g,1}$) centered around 1.6 to 1.8 eV as the nanostructures become thinner and generally confined. Surprisingly, as the nanosheets become thinner (from 104 to 37 nm), a new high-energy PL peak ($E_{g,2}$) emerges around 1.9 to 2.0 eV. In more confined and even thinner structures such as the 58 and 26 nm-thick nanowires, the intensity of the low-energy peak is consistently diminished, and the high-energy PL peak drastically increases. Based on several first-principles studies previously discussed,[50,51] we attribute the emergence of the high-energy peak to the population of the higher-energy Γ-to-Γ conduction band minimum (CBM) state, which, from the literature, was estimated to lie within 0.1 to 0.2 eV above the indirect gap (Γ-to-*Z*) CBM state.[50,51,65,66] This indirect gap CBM state corresponds to the interchain interactions of the stereochemically active Sb 5s lone pairs oriented along the *z*-axis ([001]) direction. As both the cross-sectional areas and thicknesses of the [−101]-oriented quasi-2D nanosheets and [100]-oriented nanowires decrease, the interactions along the *z*-axis that directly correspond to the indirect (Γ-to-*Z*) CBM state become increasingly suppressed. The emergence of the high-energy PL peak aligns well with the onset of suppression of the bulk indirect gap states in the *Z* point and population of higher-energy states along the Γ point originating from such confinement.

We performed AFM, micro-Raman, dark-field microscopy, and PL mapping to visualize the thickness-dependent emergence of the PL peak centered at around 1.95 eV (Figure 3f−k). Upon establishing the thicknesses and morphological uniformity of the representative nanowires using AFM and dark-field scattering microscopy (Figure 3f,h), we show that the nanowires remain crystalline through the persistence of the sharp A_g phonon mode centered at 280 cm^{-1} in the micro-Raman map (Figure 3g). Directly comparing and overlaying the PL maps derived from the 1.77 eV (yellow map; Figure 3i) and 1.95 eV (blue map; Figure 3j) peaks, we can see a clear distinction between the PL map profiles of the nanowires of various thicknesses (Figure 3i−k). Thicker nanowires displayed a brighter PL profile in the 1.77 eV spectral region, while thinner wires showed a more intense PL profile in the 1.95 eV spectral region, consistent with the emergence of a high-energy PL peak upon confinement. The *Y* + *B* overlay plot further highlights this distinction, with the pronounced blue signals corresponding to the peak centered at 1.95 eV becoming evident in thinner nanowires (Figure 3k).

To assess the size-dependent evolution of the phonon modes and PL of the Sb_2S_3 nanowires, we collected the Raman and PL spectra of isolated nanowires with various cross-sectional areas and thicknesses from 498 to 13 nm (Figure 3l). The thicknesses were measured using AFM, and the lateral dimensions were approximated using SEM imaging (Table S6). We show that the nanowires retain their crystalline order down to a 13 nm-thick nanowire based on the persistence of Raman-active Sb_2S_3 phonon modes (Figure 3l, left). We also observe a distinct blue-shift of the symmetric A_g Sb−S stretching mode from 307.5 to 311.5 cm^{-1} as the nanowires

https://doi.org/10.1021/jacs.3c05887
J. Am. Chem. Soc. 2023, 145, 22413−22424

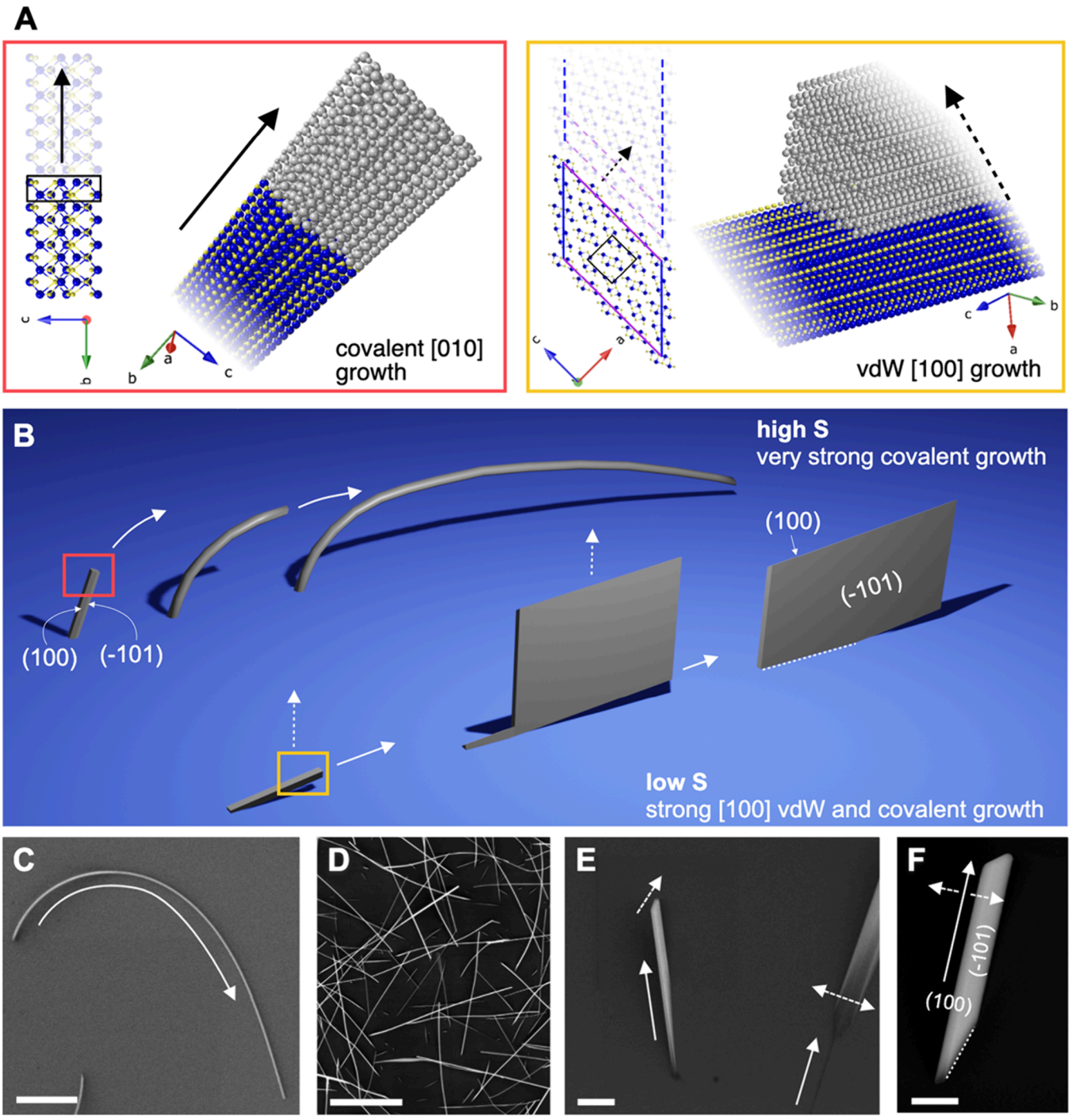

Figure 4. Experimental support for the proposed crystallization pathways of Sb_2S_3 nanocrystals. (a) Crystal structure schematic showing the two distinct Sb_2S_3 crystallographic growth directions and faceting observed in the as-grown nanostructures. The arrows indicate the crystallographic growth direction during bottom-up crystallization for both modes. The red and yellow boxes correspond to the two nuclei structures depicted in schematic in panel b. (b) 3D rendering of the two growth pathways observed in the bottom-up vapor-phase synthesis of Sb_2S_3 in the lower-temperature substrate regions. The solid arrows indicate growth along the covalent direction, while the dashed arrows indicate growth along the vdW direction. (c–f) Representative SEM images of a nanowire highlighting the covalent growth direction (c), a dense region of nanowires growing in the covalent region (d), and nanoribbons showing the growth along multiple crystallographic axes and bonding directions (e, f). Scale bars: 1 μm for panels c, e, and f and 5 μm for panel d.

become thinner, indicative of phonon confinement effects along the length of the chain. Owing to the strong bonding anisotropy in the lattice,[63] the intensities of the Raman-active peaks were strongly dependent on the orientation of the nanowires with respect to the polarization of the laser source (Figure 3l, left, and Figure S8b).

Confinement effects were also observed in the thickness-dependent PL spectra of the Sb_2S_3 nanowires (Figure 3l, right). The PL spectroscopy of the wires showed two important features that demonstrate confinement-induced evolution of the optical properties (Figure 3m). First, the lower-energy indirect band gap PL peak ($E_{g,1}$, 1.6 to 1.8 eV)[50,51,54,55]

https://doi.org/10.1021/jacs.3c05887
J. Am. Chem. Soc. 2023, 145, 22413−22424

undergoes a consistent blue-shift with decreasing thickness. Second, a new high-energy peak ($E_{g,2}$) centered around 1.9−2.0 eV, similar to what was observed in Figure 3e, emerges in nanowires thinner than 100 nm. As the nanowires became thinner, this peak also exhibited a blue-shift. Strikingly, the energy differences between these two peaks agree very well with the calculated energy differences between the indirect and direct transitions.[50,51] Furthermore, the intensity of the high-energy peak with respect to the indirect gap peak systematically increases as the cross-sectional area and thickness of the nanowires decrease. This trend becomes more apparent by looking at the intensity ratios of the $E_{g,2}$ and $E_{g,1}$ peaks (Table S6). We found that the $E_{g,2}/E_{g,1}$ peak intensity ratios consistently increase as the thicknesses and cross-sectional areas of the nanowires decrease, indicating that the higher-energy PL peak corresponding to the Γ-to-Γ transition becomes more apparent in thinner nanowires. We explain this trend by considering the consequences of suppressing growth along the *a*/*c*-plane (basal plane). The reduction in the cross-sectional area of the nanowires leads to an upshift of indirect gap states ($E_{g,1\ low}$ ∼1.6−1.8 eV) at the CBM at the *Z*-point, which is mainly induced by *c*-axis ([001] direction) quantum confinement. This confinement leads to a redistribution of excitable carriers to a higher-energy state at the Γ-point CBM, resulting in an observable, blue-shifted energy gap ($E_{g,2\ high}$ ∼1.9−2.0 eV). These results are suggestive of the beginning of a confinement-induced indirect-to-direct band gap crossover in ultrathin Sb_2S_3 nanowires. Noting the comparable intensities of the low- and high-energy PL peaks, we consider the emergence of a high-energy PL peak ($E_{g,2}$) and the systematic thickness-dependent evolution to lower values of the $Eg_{,1}/E_{g,2}$ intensity ratios as an onset feature, since it involves the systematic evolution of the low-energy and high-energy PL peaks in all samples. The lack of a precipitous increase in the intensity of $E_{g,2}$ and the observation of both PL peaks imply that the crossover from the indirect gap to the direct gap state is incomplete. Nonetheless, we note that the observed $E_{g,1}/E_{g,2}$ intensity ratios of the smallest nanowires are consistent with few-layer to bilayer transition metal dichalcogenides that exhibit the coexistence of indirect and direct gap PL peak features with comparable peak-to-peak intensities.[67,68]

Growth Pathways Leading to Dimensionally Resolved Sb_2S_3 nanostructures. With the size- and morphology-dependent properties of Sb_2S_3 nanocrystals established, we next focused on elucidating the growth pathways of these nanostructures. We took an instructive approach to understand the bonding nature and crystal faceting in the bulk orthorhombic Sb_2S_3 structure and how they translate to the resulting structure of the nanocrystals. Herein, we sought to reconcile the concept of anisotropic vdW interactions across $[Sb_4S_6]_n$ chains in the *a*/*c*-plane (basal plane) in the context of the directional CVD growth of anisotropic Sb_2S_3 nanostructures (Figure 4 and Figure S12). To this end, we determined the relative propensity for crystal growth across different lattice planes in Sb_2S_3 by analyzing the bonding interactions involved during growth along a specific crystalline facet. In our analysis, we focused on the experimentally observed low-index directions: along the observed covalent [010] growth direction (Figure 4a, left, and Figure S13), the observed vdW [100] growth direction (Figure 4a, right, and Figure S13), and the observed vdW [−101] facet direction (Figure S13). For this approach, we projected the conventional unit cell onto the respective lattice planes such that the vector of the growth direction of interest lies along one of the axes of this modified unit cell. These modified unit cells retained the stoichiometry of the conventional unit cell. Then, we qualitatively accounted for the number of covalent or vdW bonds involved in the formation of another unit cell or a quasi-2D layer of Sb_2S_3 (Figure S13 and Table S7). We assessed the propensity of different growth directions based on the strength of covalent bonds and vdW bonds formed along the growing terminal facet. Since growth along the [010] direction (Figure S13d) involves the formation of more reactive covalent bonds, we anticipate that this process will be the most favorable. In contrast, when considering the growth along the vdW-bound interchain direction, we accounted for the tendency of the facet to harbor growth similar to vdW epitaxy observed in 2D vdW crystals.[69−72] Among these interchain directions, the growth along the [100] direction (Figure S13a) involves the least number and weakest vdW interactions to grow the next layer of the material. This suggests that minimal energy is required to initiate growth, making this growth mode more favorable than along directions ([001] or [−101]), which require stronger vdW interactions to grow the next layer (Figure S13b,c). We qualitatively analyzed the crystal faceting of the resulting Sb_2S_3 nanostructures and found a good agreement with the crystal shape models that we systematically constructed based on different growth scenarios (Supplementary Section III: Additional discussion of results; Figure S12−14; Tables S7 and S8).

We applied our analysis of the hypothetical bonding- and facet-dependent progression of nanocrystal growth to rationalize the depicted deposition regions (Figure 2a,b, Figures S13 and S14, and Tables S7 and S8). The high-temperature region (>330 °C), which is also closest to the precursor region, is characterized by the abundant growth of bulk crystals (>1 μm). The growth of bulk crystals in this region is a result of uncontrolled covalent and vdW growth (Figure 2d; crystal shape B in Figure S14). High temperatures initiate and promote covalent and vdW growth modes without any preference for either growth modality. Consequently, crystal morphologies similar to naturally occurring bulk Sb_2S_3 (Stibnite) mineral were observed. In the highest-temperature region, we observed amorphous nanoparticles (Figure 2c, substrate I), suggesting that the temperature was too high to maintain ordered interactions. In contrast, the lower-temperature regions (<330 °C) of the substrates presented more distinctive growth patterns. This provided a means to resolve the morphologies of the nanocrystals based on the intrinsic anisotropy in the structure and vapor-phase precursor ratios of Sb and S (Figure 2e−g).

Two uncatalyzed growth pathways are involved in the crystallization of Sb_2S_3 nanostructures based on the assembly of $[Sb_4S_6]_n$ chains along the [010] and [100] directions (Figure 4a,b). The crystallization of Sb_2S_3 nanostructures originates from short and thin nanowire-like nuclei structures based on SEM micrographs and EDS elemental analyses of regions close to the substrate−nanostructure interface (Figure 4c−f, Figure S10−S12, and Table S4) as well as the known indexed facets in the nanostructures (Figure 2i,m,n and Figure S5). These structures, which serve as sites for subsequent crystal growth, were found to have a ∼2:3 Sb-to-S composition (Figure S10 and Table S4) and are projected slightly upward away from the substrate. In the presence of a continuous high S flux (Figure 2b, substrate IV), these nuclei elongate because of the growth along the covalent axis ([010] direction) to form

https://doi.org/10.1021/jacs.3c05887
J. Am. Chem. Soc. 2023, 145, 22413−22424

high-aspect-ratio nanowires (up to 10−15 μm in length) (Figure 4c,d, Figure S4, and crystal shape C in Figure S14). Conversely, when S was not shuttled and the vapor composition had a lower Sb-to-S ratio (Figure 2a, substrate III), these nuclei grew simultaneously in the covalent and vdW directions to form nanosheets, albeit at different rates. Subsequent [100] vdW growth begins at one of the (100) facets of the nanowire and progresses orthogonally with respect to the nanowire axis. These steps result in a vertically oriented nanosheet with [−101] facets that we observed in the form of quasi-2D nanosheets and nanoribbons (Figure 4e,f, Figure S11, and crystal shape E in Figure S14). These quasi-2D nanostructures can also be described as vertical stacks of [100]-oriented nanowires. The growth modes proposed here illustrate that the formation of anisotropic nanostructures is strongly dependent on the balance between the growth rates along the covalent and vdW directions.

The difference between the covalent and vdW growth modes can be rationalized by examining the relative amounts of Sb and S required in the vapor phase to extend the growing facet.[73,74] Comparing these two perpendicular growth directions, the growth along the chain direction requires more sulfur atoms than antimony atoms, which is consistent with the 2:3 bulk stoichiometry (Figure S13 and Table S7). When additional sulfur was shuttled during synthesis, there was a higher sulfur concentration in the vapor phase. Under these conditions, thin nanowires with several microns in length are formed since the high S vapor promotes covalent chain growth more than vdW growth (Figure 4b−d and Figures S4, S9, and S14). In contrast, growth along the vdW [100] direction, which requires fewer S atoms, was favored when sulfur was not shuttled. This resulted in the formation of short (∼1 to 2 μm-long) nanowire-like nuclei (Figure 4b,e,f and Figures S11, S12, and S14), which served as sites for vertical growth along the [100] direction, yielding quasi-2D nanoribbons and nanosheets with large exposed [−101] facets. Altogether, we determined herein that the growth of bulk and nanoscale structures derived from q-1D vdW phases is strongly influenced by the highly anisotropic bonding nature of Sb_2S_3 and is reliant on growth temperatures and ratios of the Sb and S species in the vapor phase prior to deposition.[71]

CONCLUSIONS

Overall, we established that the interplay between the strong intrachain covalency and the highly anisotropic interchain vdW interactions across 1D and q-1D vdW structures can be harnessed for the directional growth of nanowires, nanoribbons, and nanosheets at various length scales. The ability to access these diverse nanostructures has enabled the discovery of emergent size- and dimensionality-dependent photophysical properties. We anticipate that the synthetic pathways presented here are translatable to a library of solids composed of weakly bound chains. Our results highlight strategies that could advance practical use of 1D and q-1D vdW phases in polarization- and anisotropy-driven optoelectronic technologies that approach subnanometer length scales.

ASSOCIATED CONTENT

Supporting Information

The Supporting Information is available free of charge at https://pubs.acs.org/doi/10.1021/jacs.3c05887.

(Supplementary Section I) Chemical vapor deposition (CVD) setup and methodology; (Supplementary Section II) materials and characterization; (Supplementary Section III) additional discussion of results; (Supplementary Section IV) additional characterization data; (Figure S1) schematic and operational modes of the homebuilt CVD system; (Figure S2) stages of the chemical vapor deposition reaction of Sb_2S_3 nanostructures; (Figure S3) calibration of the substrate region of two-zone furnace; (Figure S4) representative SEM and STEM images of Sb_2S_3 nanowires on the growth substrate; (Figure S5) HAADF-STEM micrographs and FFTs corresponding to the EELS map in Figure 2j,o; (Figure S6) EELS spectra of the Sb_2S_3 nanostructures; (Figure S7) surface analysis of the Sb_2S_3 nanowire ensemble on the growth substrate using XPS; (Figure S8) anisotropy in bulk and nanowire Sb_2S_3; (Figure S9) elemental analysis of Sb_2S_3 nanowire ensembles on the growth substrate using SEM-EDS; (Figure S10) elemental analysis of nanowire nucleation sites via SEM-EDS; (Figure S11) elemental mapping of quasi-2D nanostructures using SEM-EDS; (Figure S12) orthorhombic crystal facets of quasi-2D Sb_2S_3 nanoribbons and nanoplates; (Figure S13) bonding interactions and stoichiometries of Sb and S in various growth modes across high symmetry crystalline axes in Sb_2S_3; (Figure S14) qualitative visualization of the different combinations of crystal facet growth propensities guided by the hypothetical crystal shape models of Sb_2S_3; (Table S1) list of components of the chemical vapor deposition system in Figure S1; (Table S2) summary of Sb_2S_3 XPS peak parameters fitted using the CasaXPS software; (Table S3) atomic composition of Sb_2S_3 nanowire ensembles in Figure S9; (Table S4) atomic composition of the nanowire nucleation sites in Figure S10; (Table S5) atomic composition of the Sb_2S_3 quasi-2D nanoribbons and nanosheets in Figure S11; (Table S6) height, width, and cross-sectional analysis of isolated Sb_2S_3 nanowires used in single nanowire studies (Figure 3l); (Table S7) qualitative account of the bonding interactions formed during each growth mode; (Table S8) structural parameters of the hypothetical crystal shape models from Figure S14 (PDF)

AUTHOR INFORMATION

Corresponding Author

Maxx Q. Arguilla − *Department of Chemistry, University of California Irvine, Irvine, California 92697, United States;* orcid.org/0000-0001-9948-0814; Email: marguill@uci.edu

Authors

Dmitri Leo Mesoza Cordova − *Department of Chemistry, University of California Irvine, Irvine, California 92697, United States*

Kenneth Chua − *Department of Chemistry, University of California Irvine, Irvine, California 92697, United States*

Rebecca Mai Huynh − *Department of Chemistry, University of California Irvine, Irvine, California 92697, United States*

Toshihiro Aoki − *Irvine Materials Research Institute, University of California Irvine, Irvine, California 92697, United States;* orcid.org/0000-0001-6620-9390

https://doi.org/10.1021/jacs.3c05887
J. Am. Chem. Soc. 2023, 145, 22413−22424

Complete contact information is available at:
https://pubs.acs.org/10.1021/jacs.3c05887

Notes

The authors declare no competing financial interest.

■ ACKNOWLEDGMENTS

We thank the UC Irvine Department of Chemistry Laser Spectroscopy Laboratories. Several aspects of this work were performed at the UC Irvine Materials Research Institute (IMRI). Facilities and instrumentation at IMRI are supported, in part, by the National Science Foundation through the UC Irvine Materials Research Science and Engineering Center grant number DMR-2011967. XPS was performed using instrumentation funded in part by the National Science Foundation Major Research Instrumentation Program under grant number CHE-1338173. AFM was performed using an Anton Paar Tosca 400 AFM on loan to IMRI from Anton Paar GmbH.

■ REFERENCES

(1) Geim, A. K.; Novoselov, K. S. The rise of graphene. *Nat. Mater.* **2007**, *6* (3), 183−191.
(2) Island, J. O.; Molina-Mendoza, A. J.; Barawi, M.; Biele, R.; Flores, E.; Clamagirand, J. M.; Ares, J. R.; Sanchez, C.; van der Zant, H. S. J.; D'Agosta, R. Electronics and optoelectronics of quasi-1D layered transition metal trichalcogenides. *2D Mater.* **2017**, *4* (2), No. 022003.
(3) Mak, K. F.; Shan, J. Photonics and optoelectronics of 2D semiconductor transition metal dichalcogenides. *Nat. Photonics* **2016**, *10* (4), 216−226.
(4) Mannix, A. J.; Kiraly, B.; Hersam, M. C.; Guisinger, N. P. Synthesis and chemistry of elemental 2D materials. *Nat. Rev. Chem.* **2017**, *1* (2), No. 0014.
(5) Schaibley, J. R.; Yu, H.; Clark, G.; Rivera, P.; Ross, J. S.; Seyler, K. L.; Yao, W.; Xu, X. Valleytronics in 2D materials. *Nat. Rev. Mater.* **2016**, *1* (11), 16055.
(6) Zhu, Y. B.; Rehn, D. A.; Antoniuk, E. R.; Cheon, G.; Freitas, R.; Krishnapriyan, A.; Reed, E. J. Spectrum of exfoliable 1D van der Waals molecular wires and their electronic properties. *ACS Nano* **2021**, *15* (6), 9851−9859.
(7) Balandin, A. A.; Kargar, F.; Salguero, T. T.; Lake, R. K. One-dimensional van der Waals quantum materials. *Mater. Today* **2022**, *55*, 74−91.
(8) Roy, X.; Lee, C. H.; Crowther, A. C.; Schenck, C. L.; Besara, T.; Lalancette, R. A.; Siegrist, T.; Stephens, P. W.; Brus, L. E.; Kim, P.; Steigerwald, M. L.; Nuckolls, C.; et al. Nanoscale atoms in solid-state chemistry. *Science* **2013**, *341* (6142), 157−160.
(9) Tao, A. R.; Habas, S.; Yang, P. Shape control of colloidal metal nanocrystals. *Small* **2008**, *4* (3), 310−325.
(10) Bierman, M. J.; Lau, Y. K. A.; Kvit, A. V.; Schmitt, A. L.; Jin, S. Dislocation-driven nanowire growth and Eshelby twist. *Science* **2008**, *320* (5879), 1060−1063.
(11) Liu, Y.; Wang, J.; Kim, S.; Sun, H.; Yang, F.; Fang, Z.; Tamura, N.; Zhang, R.; Song, X.; Wen, J.; Xu, B. Z.; Wang, M.; Lin, S.; Yu, Q.; Tom, K. B.; Deng, Y.; Turner, J.; Chan, E.; Jin, D.; Ritchie, R. O.; Minor, A. M.; Chrzan, D. C.; Scott, M. C.; Yao, J. Helical van der Waals crystals with discretized Eshelby twist. *Nature* **2019**, *570* (7761), 358−362.
(12) Liu, C.; Wang, Y.; Li, H.; Wu, Y.; Li, Y.; Li, J.; He, K.; Xu, Y.; Zhang, J.; Wang, Y. Robust axion insulator and Chern insulator phases in a two-dimensional antiferromagnetic topological insulator. *Nat. Mater.* **2020**, *19* (5), 522−527.
(13) Tang, L.; Tan, J.; Nong, H.; Liu, B.; Cheng, H.-M. Chemical vapor deposition growth of two-dimensional compound materials: controllability, material quality, and growth mechanism. *Acc. Mater. Res.* **2021**, *2* (1), 36−47.
(14) Novoselov, K. S.; Jiang, Z.; Zhang, Y.; Morozov, S. V.; Stormer, H. L.; Zeitler, U.; Maan, J. C.; Boebinger, G. S.; Kim, P.; Geim, A. K. Room-temperature quantum hall effect in graphene. *Science* **2007**, *315* (5817), 1379−1379.
(15) Zhang, Y.; Tan, Y. W.; Stormer, H. L.; Kim, P. Experimental observation of the quantum Hall effect and Berry's phase in graphene. *Nature* **2005**, *438* (7065), 201−204.
(16) Cao, Y.; Fatemi, V.; Fang, S.; Watanabe, K.; Taniguchi, T.; Kaxiras, E.; Jarillo-Herrero, P. Unconventional superconductivity in magic-angle graphene superlattices. *Nature* **2018**, *556* (7699), 43−50.
(17) Deng, Y.; Yu, Y.; Shi, M. Z.; Guo, Z.; Xu, Z.; Wang, J.; Chen, X. H.; Zhang, Y. Quantum anomalous Hall effect in intrinsic magnetic topological insulator $MnBi_2Te_4$. *Science* **2020**, *367* (6480), 895−900.
(18) Lee, J.; Mak, K. F.; Shan, J. Electrical control of the valley Hall effect in bilayer MoS_2 transistors. *Nat. Nanotechnol.* **2016**, *11* (5), 421−425.
(19) So, J. P.; Kim, H. R.; Baek, H.; Jeong, K. Y.; Lee, H. C.; Huh, W.; Kim, Y. S.; Watanabe, K.; Taniguchi, T.; Kim, J.; Lee, C. H.; Park, H. G. Electrically driven strain-induced deterministic single-photon emitters in a van der Waals heterostructure. *Sci. Adv.* **2021**, *7* (43), No. eabj3176.
(20) Chowdhury, T.; Kim, J.; Sadler, E. C.; Li, C.; Lee, S. W.; Jo, K.; Xu, W.; Gracias, D. H.; Drichko, N. V.; Jariwala, D.; Brintlinger, T. H.; Mueller, T.; Park, H. G.; Kempa, T. J. Substrate-directed synthesis of MoS_2 nanocrystals with tunable dimensionality and optical properties. *Nat. Nanotechnol.* **2020**, *15* (1), 29−34.
(21) Li, S.; Lin, Y. C.; Zhao, W.; Wu, J.; Wang, Z.; Hu, Z.; Shen, Y.; Tang, D. M.; Wang, J.; Zhang, Q.; Zhu, H.; Chu, L.; Zhao, W.; Liu, C.; Sun, Z.; Taniguchi, T.; Osada, M.; Chen, W.; Xu, Q. H.; Wee, A. T. S.; Suenaga, K.; Ding, F.; Eda, G. Vapour-liquid-solid growth of monolayer MoS_2 nanoribbons. *Nat. Mater.* **2018**, *17* (6), 535−542.
(22) Xu, H.; Liu, S.; Ding, Z.; Tan, S. J. R.; Yam, K. M.; Bao, Y.; Nai, C. T.; Ng, M. F.; Lu, J.; Zhang, C.; Loh, K. P. Oscillating edge states in one-dimensional MoS_2 nanowires. *Nat. Commun.* **2016**, *7*, 12904.
(23) Aljarb, A.; Fu, J. H.; Hsu, C. C.; Chuu, C. P.; Wan, Y.; Hakami, M.; Naphade, D. R.; Yengel, E.; Lee, C. J.; Brems, S.; Chen, T. A.; Li, M. Y.; Bae, S. H.; Hsu, W. T.; Cao, Z.; Albaridy, R.; Lopatin, S.; Chang, W. H.; Anthopoulos, T. D.; Kim, J.; Li, L. J.; Tung, V. Ledge-directed epitaxy of continuously self-aligned single-crystalline nanoribbons of transition metal dichalcogenides. *Nat. Mater.* **2020**, *19* (12), 1300−1306.
(24) Xiang, R.; Inoue, T.; Zheng, Y.; Kumamoto, A.; Qian, Y.; Sato, Y.; Liu, M.; Tang, D.; Gokhale, D.; Guo, J.; Hisama, K.; Yotsumoto, S.; Ogamoto, T.; Arai, H.; Kobayashi, Y.; Zhang, H.; Hou, B.; Anisimov, A.; Maruyama, M.; Miyata, Y.; Okada, S.; Chiashi, S.; Li, Y.; Kong, J.; Kauppinen, E. I.; Ikuhara, Y.; Suenaga, K.; Maruyama, S.; et al. One-dimensional van der Waals heterostructures. *Science* **2020**, *367* (6477), 537−542.
(25) Autès, G.; Isaeva, A.; Moreschini, L.; Johannsen, J. C.; Pisoni, A.; Mori, R.; Zhang, W.; Filatova, T. G.; Kuznetsov, A. N.; Forró, L.; Van den Broek, W.; Kim, Y.; Kim, K. S.; Lanzara, A.; Denlinger, J. D.; Rotenberg, E.; Bostwick, A.; Grioni, M.; Yazyev, O. V. A novel quasi-one-dimensional topological insulator in bismuth iodide β-Bi_4I_4. *Nat. Mater.* **2016**, *15* (2), 154−158.
(26) Lin, C.; Ochi, M.; Noguchi, R.; Kuroda, K.; Sakoda, M.; Nomura, A.; Tsubota, M.; Zhang, P.; Bareille, C.; Kurokawa, K.; Arai, Y.; Kawaguchi, K.; Tanaka, H.; Yaji, K.; Harasawa, A.; Hashimoto, M.; Lu, D.; Shin, S.; Arita, R.; Tanda, S.; Kondo, T.; et al. Visualization of the strain-induced topological phase transition in a quasi-one-dimensional superconductor $TaSe_3$. *Nat. Mater.* **2021**, *20* (8), 1093−1099.
(27) Shumiya, N.; Hossain, M. S.; Yin, J. X.; Wang, Z.; Litskevich, M.; Yoon, C.; Li, Y.; Yang, Y.; Jiang, Y. X.; Cheng, G.; Lin, Y. C.; Zhang, Q.; Cheng, Z. J.; Cochran, T. A.; Multer, D.; Yang, X. P.; Casas, B.; Chang, T. R.; Neupert, T.; Yuan, Z.; Jia, S.; Lin, H.; Yao, N.; Balicas, L.; Zhang, F.; Yao, Y.; Hasan, M. Z.; et al. Evidence of a room-temperature quantum spin Hall edge state in a higher-order topological insulator. *Nat. Mater.* **2022**, *21* (10), 1111−1115.

(28) Liu, G.; Rumyantsev, S.; Bloodgood, M. A.; Salguero, T. T.; Shur, M.; Balandin, A. A. Low-frequency electronic noise in quasi-1D $TaSe_3$ van der Waals nanowires. *Nano Lett.* **2017**, *17* (1), 377−383.
(29) Fu, B.; Wang, H. W.; Shen, S. Q. Dirac polarons and resistivity anomaly in $ZrTe_5$ and $HfTe_5$. *Phys. Rev. Lett.* **2020**, *125* (25), No. 256601.
(30) Li, J.; Niu, Y.; Zeng, J.; Wang, J.; Wang, Q.; Liu, X.; Li, H.; de Rooij, N. F.; Wang, Y.; Zhou, G. Electrochemical exfoliation of naturally occurring layered mineral Stibnite (Sb_2S_3) for highly sensitive and fast room-temperature acetone sensing. *Adv. Mater. Interfaces* **2022**, *9* (19), 2200605.
(31) Lipatov, A.; Loes, M. J.; Lu, H.; Dai, J.; Patoka, P.; Vorobeva, N. S.; Muratov, D. S.; Ulrich, G.; Kästner, B.; Hoehl, A.; Ulm, G.; Zeng, X. C.; Rühl, E.; Gruverman, A.; Dowben, P. A.; Sinitskii, A. Quasi-1D TiS_3 nanoribbons: Mechanical exfoliation and thickness-dependent Raman spectroscopy. *ACS Nano* **2018**, *12* (12), 12713−12720.
(32) Qu, Y.; Arguilla, M. Q.; Zhang, Q.; He, X.; Dincă, M. Ultrathin, high-aspect ratio, and free-standing magnetic nanowires by exfoliation of ferromagnetic quasi-one-dimensional van der Waals lattices. *J. Am. Chem. Soc.* **2021**, *143* (46), 19551−19558.
(33) Tan, S. M.; Mayorga-Martinez, C. C.; Sofer, Z.; Pumera, M. Bipolar electrochemistry exfoliation of layered metal chalcogenides Sb_2S_3 and Bi_2S_3 and their hydrogen evolution applications. *Chem.—Eur. J.* **2020**, *26* (29), 6479−6483.
(34) Wang, M.; Xu, X.; Ge, Y.; Dong, P.; Baines, R.; Ajayan, P. M.; Ye, M.; Shen, J. Surface tension components ratio: An efficient parameter for direct liquid phase exfoliation. *ACS Appl. Mater. Interfaces* **2017**, *9* (10), 9168−9175.
(35) Zhou, Y.; Wang, L.; Chen, S.; Qin, S.; Liu, X.; Chen, J.; Xue, D. J.; Luo, M.; Cao, Y.; Cheng, Y.; Sargent, E. H.; Tang, J. Thin-film Sb_2Se_3 photovoltaics with oriented one-dimensional ribbons and benign grain boundaries. *Nat. Photonics* **2015**, *9* (6), 409−415.
(36) Malakooti, R.; Cademartiri, L.; Migliori, A.; Ozin, G. A. Ultrathin Sb_2S_3 nanowires and nanoplatelets. *J. Mater. Chem.* **2008**, *18* (1), 66−69.
(37) Yang, J.; Liu, Y. C.; Lin, H. M.; Chen, C. C. A chain-structure nanotube: growth and characterization of single-crystal Sb_2S_3 nanotubes via a chemical vapor transport reaction. *Adv. Mater.* **2004**, *16* (8), 713−716.
(38) Ye, K.; Wang, B.; Nie, A.; Zhai, K.; Wen, F.; Mu, C.; Zhao, Z.; Xiang, J.; Tian, Y.; Liu, Z. Broadband photodetector of high quality Sb_2S_3 nanowire grown by chemical vapor deposition. *J. Mater. Sci. Technol.* **2021**, *75*, 14−20.
(39) Bloodgood, M. A.; Ghafouri, Y.; Wei, P.; Salguero, T. T. Impact of the chemical vapor transport agent on polymorphism in the quasi-1D NbS_3 system. *Appl. Phys. Lett.* **2022**, *120* (17), 173103.
(40) Kondrotas, R.; Chen, C.; Tang, J. Sb_2S_3 solar cells. *Joule* **2018**, *2* (5), 857−878.
(41) Rhee, J. H.; Chung, C.-C.; Diau, E. W.-G. A perspective of mesoscopic solar cells based on metal chalcogenide quantum dots and organometal-halide perovskites. *NPG Asia Mater.* **2013**, *5* (10), No. e68.
(42) Choi, Y. C.; Lee, D. U.; Noh, J. H.; Kim, E. K.; Seok, S. I. Highly improved Sb_2S_3 sensitized-inorganic−organic heterojunction solar cells and quantification of traps by deep-level transient spectroscopy. *Adv. Funct. Mater.* **2014**, *24* (23), 3587−3592.
(43) Zhang, H.; Yuan, S.; Deng, H.; Ishaq, M.; Yang, X.; Hou, T.; Shah, U. A.; Song, H.; Tang, J. Controllable orientations for Sb_2S_3 solar cells by vertical VTD method. *Prog. Photovoltaics: Res. Appl.* **2020**, *28* (8), 823−832.
(44) Deng, H.; Cheng, Y.; Chen, Z.; Lin, X.; Wu, J.; Zheng, Q.; Zhang, C.; Cheng, S. Flexible substrate-structured Sb_2S_3 solar cells with back interface selenization. *Adv. Funct. Mater.* **2023**, *33*, 2212627.
(45) Peng, Z.; Zheng, Q.; Wang, R.; Sun, L.; Wang, H.; Yuan, Y.; Xing, Y.; Yao, L.; Bi, J.; Li, W. Controllable (hk1) preferred orientation of Sb_2S_3 thin films fabricated by pulse electrodeposition. *Sol. Energy Mater. Sol. Cells* **2023**, *253*, No. 112208.
(46) Grad, L.; von Rohr, F. O.; Hengsberger, M.; Osterwalder, J. Charge carrier dynamics and self-trapping on Sb_2S_3 (100). *Phys. Rev. Mater.* **2021**, *5* (7), No. 075401.
(47) Dong, W.; Liu, H.; Behera, J. K.; Lu, L.; Ng, R. J. H.; Sreekanth, K. V.; Zhou, X.; Yang, J. K. W.; Simpson, R. E. Wide bandgap phase change material tuned visible photonics. *Adv. Funct. Mater.* **2019**, *29* (6), 1806181.
(48) Karguppikar, A.; Vedeshwar, A. Thickness dependence of the forbidden energy gap in Stibnite (Sb_2S_3) thin films. *Phys. Lett. A* **1987**, *126* (2), 123−126.
(49) Mane, R. S.; Lokhande, C. D. Thickness-dependent properties of chemically deposited Sb_2S_3 thin films. *Mater. Chem. Phys.* **2003**, *82* (2), 347−354.
(50) Caruso, F.; Filip, M. R.; Giustino, F. Excitons in one-dimensional van der Waals materials: Sb_2S_3 nanoribbons. *Phys. Rev. B* **2015**, *92* (12), No. 125134.
(51) Peng, Y.; Xia, C.; Tan, Z.; An, J.; Zhang, Q. Size-controlled excitonic effects on electronic and optical properties of Sb_2S_3 nanowires. *Phys. Chem. Chem. Phys.* **2019**, *21* (48), 26515−26524.
(52) Bayliss, P.; Nowacki, W. Refinement of crystal structure of Stibnite, Sb_2S_3. *Z. Kristallogr. Cryst. Mater.* **1972**, *135* (3−6), 308−315.
(53) Kyono, A.; Kimata, M.; Matsuhisa, M.; Miyashita, Y.; Okamoto, K. Low-temperature crystal structures of Stibnite implying orbital overlap of Sb $5s^2$ inert pair electrons. *Phys. Chem. Miner.* **2002**, *29* (4), 254−260.
(54) Wang, X.; Li, Z.; Kavanagh, S. R.; Ganose, A. M.; Walsh, A. Lone pair driven anisotropy in antimony chalcogenide semiconductors. *Phys. Chem. Chem. Phys.* **2022**, *24* (12), 7195−7202.
(55) Carey, J. J.; Allen, J. P.; Scanlon, D. O.; Watson, G. W. The electronic structure of the antimony chalcogenide series: Prospects for optoelectronic applications. *J. Solid State Chem.* **2014**, *213*, 116−125.
(56) Okamoto, H. *Desk handbook: phase diagrams for binary alloys*; ASM international, 2000.
(57) Lee, Y. H.; Itagaki, K. Thermodynamic study of liquid Sb−S and Sb_2S_3−FeS systems by the use of a drop-calorimeter. *Trans. Jpn. Inst. Met.* **1986**, *27* (12), 987−995.
(58) Zhang, Z.; Chen, P.; Duan, X.; Zang, K.; Luo, J.; Duan, X. Robust epitaxial growth of two-dimensional heterostructures, multiheterostructures, and superlattices. *Science* **2017**, *357* (6353), 788−792.
(59) Wagner, R. S.; Ellis, W. C. Vapor-liquid-solid mechanism of single crystal growth. *Appl. Phys. Lett.* **1964**, *4* (5), 89−90.
(60) Ambrosini, S.; Fanetti, M.; Grillo, V.; Franciosi, A.; Rubini, S. Vapor-liquid-solid and vapor-solid growth of self-catalyzed GaAs nanowires. *AIP Advances* **2011**, *1* (4), No. 042142.
(61) Meyers, J. K.; Kim, S.; Hill, D. J.; Cating, E. E. M.; Williams, L. J.; Kumbhar, A. S.; McBride, J. R.; Papanikolas, J. M.; Cahoon, J. F. Self-catalyzed vapor−liquid−solid growth of lead halide nanowires and conversion to hybrid perovskites. *Nano Lett.* **2017**, *17* (12), 7561−7568.
(62) Abe, M.; Suzuki, R.; Kojima, K.; Tachibana, M. Evaluation of crystal quality of thin protein crystals based on the dynamical theory of X-ray diffraction. *IUCrJ.* **2020**, *7* (4), 761−766.
(63) Sereni, P.; Musso, M.; Knoll, P.; Blaha, P.; Schwarz, K.; Schmidt, G. Polarization-dependent raman characterization of Stibnite (Sb_2S_3). *Am. Inst. Phys. Vol.* **2010**, *1267*, 1131−1132, DOI: 10.1063/1.3482339.
(64) Liu, Y.; Chua, K. T. E.; Sum, T. C.; Gan, C. K. First-principles study of the lattice dynamics of Sb_2S_3. *Phys. Chem. Chem. Phys.* **2014**, *16* (1), 345−350.
(65) Mishra, R. K.; Vedeshwar, A. G.; Tandon, R. P. Sb_2S_3 quantum dots: diffusion-controlled growth and characterization. *Phys. Status Solidi RRL* **2013**, *7* (11), 975−979.
(66) Variano, B. F.; Hwang, D. M.; Sandroff, C. J.; Wiltzius, P.; Jing, T. W.; Ong, N. P. Quantum effects in anisotropic semiconductor clusters: Colloidal suspensions of bismuth sesquisulfide and antimony sesquisulfide. *J. Phys. Chem.* **1987**, *91* (26), 6455−6458.

(67) Ernandes, C.; Khalil, L.; Almabrouk, H.; Pierucci, D.; Zheng, B.; Avila, J.; Dudin, P.; Chaste, J.; Oehler, F.; Pala, M.; Bisti, F.; Lhuillier, E.; Pan, A.; Ouerghi, A. Indirect to direct band gap crossover in two-dimensional $WS_{2(1-x)}Se_{2x}$ alloys. *npj 2D Mater. Appl.* **2021**, *5* (1), 7.
(68) Mak, K. F.; Lee, C.; Hone, J.; Shan, J.; Heinz, T. F. Atomically thin MoS_2: A new direct-gap semiconductor. *Phys. Rev. Lett.* **2010**, *105* (13), No. 136805.
(69) Govind Rajan, A.; Warner, J. H.; Blankschtein, D.; Strano, M. S. Generalized mechanistic model for the chemical vapor deposition of 2D transition metal dichalcogenide monolayers. *ACS Nano* **2016**, *10* (4), 4330−4344.
(70) Shang, S.-L.; Lindwall, G.; Wang, Y.; Redwing, J. M.; Anderson, T.; Liu, Z.-K. Lateral versus vertical growth of two-dimensional layered transition-metal dichalcogenides: thermodynamic insight into MoS_2. *Nano Lett.* **2016**, *16* (9), 5742−5750.
(71) Wang, S.; Rong, Y.; Fan, Y.; Pacios, M.; Bhaskaran, H.; He, K.; Warner, J. H. Shape evolution of monolayer MoS_2 crystals grown by chemical vapor deposition. *Chem. Mater.* **2014**, *26* (22), 6371−6379.
(72) Mortelmans, W.; De Smet, K.; Meng, R.; Houssa, M.; De Gendt, S.; Heyns, M.; Merckling, C. Role of stronger interlayer van der Waals coupling in twin-free molecular beam epitaxy of 2D chalcogenides. *Adv. Mater. Interfaces* **2021**, *8* (13), 2100438.
(73) Padilla, R.; Ramírez, G.; Ruiz, M. C. High-temperature volatilization mechanism of Stibnite in nitrogen-oxygen atmospheres. *Metall. Mater. Trans. B* **2010**, *41*, 1284−1292.
(74) Piacente, V.; Scardala, P.; Ferro, D. Study of the vaporization behaviour of Sb_2S_3 and Sb_2Te_3 from their vapour pressure measurements. *J. Alloys Compd.* **1992**, *178* (1−2), 101−115.

https://doi.org/10.1021/jacs.3c05887
J. Am. Chem. Soc. 2023, 145, 22413−22424